Creep enhancement and sliding in a temperate, hard-bedded alpine glacier

Juan P. Roldán-Blasco[1], Adrien Gilbert[1], Luc Piard[1], Florent Gimbert[1], Christian Vincent[1], Olivier Gagliardini[1], Anuar Togaibekov[1,2], Andrea Walpersdorf[2], and Nathan Maier[1]

[1]IGE, Univ. Grenoble Alpes, CNRS, INRAE, IRD, Grenoble INP, 38000 Grenoble, France
[2]ISTerre, Univ. Grenoble Alpes, CNRS, IRD, UGE, 38000 Grenoble, France

Correspondence: Adrien Gilbert (adrien.gilbert@univ-grenoble-alpes.fr)

Abstract. Glacier internal deformation is usually described by Glen's Law using two material parameters, the creep factor A and the flow law exponent n. However, the values of these parameters and their spatial and temporal variability are rather uncertain due to the difficulty of quantifying internal strain and stress fields at the natural scale. In this study, we combine 1-year long continuous measurements of borehole inclinometry and surface velocity with three-dimensional full Stokes ice flow modeling to infer ice rheology and sliding velocity in the ablation zone of the Argentière Glacier, a temperate glacier in the French Alps. We demonstrate that the observed deformation rate profile has limited sensitivity to the flow law exponent n and instead mainly reflects an increase in the creep factor A with depth, with A departing from its surface value by at least up to a factor of 2.5 below 160 m. We interpret this creep factor enhancement as an effect of increasing interstitial water content with depth from 0% to 1.3% which results in an average value of $A = 148$ MPa^{-3} a^{-1}. We further observe that internal ice deformation exhibits seasonal variability similar to that in surface velocity, such that the local basal sliding velocity exhibits no significant seasonal variation. We suggest that these changes in deformation rate are due to variations in the stress field driven by contrasting changes in subglacial hydrology conditions between the side and the center of the glacier. Our study gives further evidence that borehole inclinometry combined with full-Stokes flow model allows constraining both ice rheology and basal friction at scales that cannot be inferred from surface velocity measurements alone.

1 Introduction

Glacier dynamics depends on both internal deformation and basal sliding. Given the scarcity of direct observations of ice rheology and basal sliding speed at the natural scale, ice flow models commonly use inverse methods to estimate the material parameters that allow ~~the best fit to the surface velocity~~ best fitting surface velocities (e.g. Arthern and Gudmundsson, 2010; Fürst et al., 2015; Mosbeux et al., 2016). However, the problem is largely undetermined due to poor knowledge of ice thickness and does not allow the identification of model weaknesses, as model errors are compensated by material parameter adjustments. Independent and accurate estimates of ice material parameters as well as sub-glacial basal friction changes are key in order to better represent glacier dynamics in models, in particular the fraction of surface velocities that is due to basal sliding versus that due to internal ice deformation.

Ice deformation is ~~known~~ commonly assumed to follow Glen's flow law (Glen, 1955), with the creep parameter A being pri-
marily dependent on ice temperature (Barnes et al., 1971; Weertman, 1983). Such dependency has been studied extensively in
both the laboratory and the field (Cuffey and Paterson, 2010), and can reasonably well be accounted for in models given a tem-
perature profile. Typical values for ice viscosity and exponents for temperate glaciers and ice-caps are $A \approx 75$ MPa^{-3} a^{-1} and
$n = 3$, respectively (Cuffey and Paterson, 2010). The applicability of these values to describe glacier dynamics at the natural
~~scales~~scale, however, is still quite uncertain, mainly as a result of other controls coming into play, such as ice texture (orientation
and microstructure, ~~(Barnes et al., 1971; Goldsby and Kohlstedt, 2001))~~(Barnes et al., 1971; Goldsby and Kohlstedt, 2001; Chauve et al., ?
, impurities (Jones and Glen, 1969) or water content (Lliboutry and Duval, 1985; Duval, 1977). These controls are chal-
lenging to evaluate as they may vary quite extensively in time and space depending on stress and deformation conditions
~~(Chauve et al., 2024a; Rathmann and Lilien, 2022)~~(Chauve et al., 2024b; Rathmann and Lilien, 2022). This is especially true
under temperate ice conditions, which are hard to ~~investigate~~ study in the laboratory where water content is difficult to control,
but also hard to characterize in the field, ~~since radar observations traditionally used to recover ice texture (Young et al., 2021)~~
~~and potentially water content (Ogier et al., 2023) are~~ requiring drilling of ice cores or indirect geophysical measurements that
are often difficult to interpret~~due to large wave scattering under temperate ice conditions. Nevertheless, in many settings ,~~.
Geophysical methods include ground penetrating radar observations (Young et al., 2021; Ogier et al., 2023), seismic tomography
(Benjumea et al., 2003; Endres et al., 2009) and surface nuclear magnetic resonance (Legchenko et al., 2014). However, the
former is mainly sensitive to integrated water content and its spatial variations are poorly retrieved. Analysis of seismic and
radar wave velocities provides relevant information on relative changes in water content but remains more uncertain in absolute
terms (Murray et al., 2007). We note that the recent use of fiber optics in boreholes provides accurate variations of seismic
velocity with depth, and might be a promising method for in-situ characterization of temperate ice properties, although yet it
has only mostly been applied to cold ice settings (Fichtner et al., 2023; Booth et al., 2020). As temperate ice deformation is
expected to primarily control ice dynamics, including on ice-sheets like Greenland where most of the deformation concentrates
in the basal temperate layer (Law et al., 2023), it is central to study it specifically.

Basal sliding on hard beds is also known to be a function of ice deformation as it is enhanced near the bed, thus with the
same sources of uncertainty as presented above, but with the added complexity that subglacial hydrology also affects it. Water
pockets, commonly referred to as cavities, can form in the lee side of bedrock bumps, reducing the apparent bed roughness,
facilitating creep and thus enhancing basal sliding (Lliboutry, 1959, 1968). Subglacial channels can also form under sufficient
turbulent-induced melt, causing the opposite effect of reducing the basal sliding through lowering the basal water pressure
(Röthlisberger, 1972; Schoof, 2010). Ultimately, the resultant effect of subglacial hydrology on overall glacier dynamics thus
depends on the type of subglacial hydrology system at play at any given time and location. Of fundamental importance is the
ability to evaluate the spatio-temporal evolution of basal sliding to improve our representation of the evolution of subglacial
hydrology and its link to overall glacier dynamics in glacier and ice-sheet models.

~~A unique means~~ Borehole inclinometry is a unique mean to investigate ice deformation and basal sliding simultaneously~~is~~
~~through borehole inclinometry~~, either by measuring the change in borehole orientation through repeated surveys (e.g. Perutz,
1949; Shreve and Sharp, 1970; Raymond, 1971; Hooke, 1973; Hooke and Hanson, 1986; Hooke et al., 1992; Harper et al., 2001;

Marshall et al., 2002; Chandler et al., 2008) or through continuous englacial tiltmeter recording (e.g. Gudmundsson et al., 1999; Lüthi et al., 2002; Willis et al., 2003; Amundson et al., 2006; Ryser et al., 2014; Keller and Blatter, 2012; Doyle et al., 2018; Lee et al., 2019; Maier et al., 2019, 2021). These observations provide deformation rate profiles that can allow in-situ estimates of the ice rheology, basal velocity and their respective temporal variations, with basal velocity obtained through integrating the deformation rate profile with depth and removing it from the surface velocity ~~obtained from GPS~~ (Hooke et al., 1992; Maier et al., 2021). However, a major challenge in evaluating ice rheology based on these observations is the retrieval of the stress field against which deformation rates can be compared. Since ~~stresses~~ stress variations with depth along the borehole cannot be measured, they must be estimated independently using a modeling approach, which, depending on model assumptions or prescribed boundary conditions, can introduce large uncertainties in the derived creep factor or flow exponent, especially in valley glaciers (e.g. Harper et al., 2001; Chandler et al., 2008) where the highly three-dimensional geometry requires an evaluation of the full stress tensor. Even on large ice caps, strong spatial variations in the measured deformation rate between different boreholes have been shown to reflect a complex stress field influenced by spatial variability in bed friction (Ryser et al., 2014), which, together with variations in ice temperature, complicates accurate assessment of ice rheology. The stress field complexity can also influence the temporal variation that can be observed in deformation rate either due to flow over a changing bed topography (Maier et al., 2019) or due to hydrologically-driven temporal changes in basal drag patterns (Hooke et al., 1992; Willis et al., 2003).

In this paper, we ~~attempt to~~ infer internal rheological parameters and reconstruct basal velocity through time by combining continuous borehole inclinometry observations with full Stokes 3-dimensional modeling of the stress field over a full melting season. The study focuses on the Argentière Glacier (temperate ice, French Alps), which has been intensively monitored for several decades (mass balance, surface velocities and topography, sliding velocity, bedrock geometry) and provides a unique and well-constrained environment for a natural scale study of ice deformation. We first describe the study site and the measurement methods. We then analyse ~~the observation~~ our observations in terms of material parameters using the flow model and finally provide the observed time series of both deformation and basal velocities. With this methodology we identify a depth-dependency of ice viscosity, which we attribute to changes in interstitial water content, as well as temporal changes in ice deformation, which we argue are due to subglacial-hydrology driven changes in basal friction conditions. These novel observations contribute to a better understanding of the complex interplay between basal sliding and internal ice deformation, while providing ~~a rare constraint~~ constraints on ice rheology in a natural setting.

2 Field site and instrumentation

2.1 The Argentière Glacier

The Argentière Glacier is a temperate glacier located in the Mont Blanc range, French Alps (45°10 N, 6°10 E). The glacier rests on a hard bedrock (Vivian and Bocquet, 1973) and extends for 9 km within an altitude range of 1600 m to 3400 m, separated by an icefall at 2300 m. ~~The dynamics of the glacier~~ Glacier dynamics has been continuously monitored since the 1970's, in particular its basal sliding velocities, thanks to direct access to the glacier bed 700 m downstream of the drilling

site (Vincent and Moreau, 2016; Gimbert et al., 2021a; Gilbert et al., 2022). The measurements are made by a cavitometer installed in a natural ice cavity that records sliding velocity at a half-hour resolution. Surface ~~dynamics shows a seasonal pattern typical of mountain glaciers, with low velocity between September and April, followed by a period of sustained high velocity between May and August~~ velocities show a seasonal variability materialized by lowest velocities in autumn (October-November) and sustained high velocities over summer (June-August) (Vincent et al., 2022). The glacier also benefits of subglacial runoff monitoring by the power company Electricité d'Emosson SA and continuous records of yearly surface mass balance, topography and velocity from the GLACIOCLIM monitoring program (https://glacioclim.osug.fr/). Several campaigns of ground penetrating radar ~~measurement~~ measurements also provide a good knowledge of ~~the basal topography (Rabatel et al., 2018; Sergeant et al., 2020; Gimbert et al., 2021b)~~ basal topography (Rabatel et al., 2018; Gimbert et al., 2021b), further extended by seismic investigations (Sergeant et al., 2020).

2.2 Borehole deformation instrumentation

Drilling operations took place between the 12th and the 14th of September 2019. The drilling sites are located in the central part of the ablation area ~~, between 600 and 800 m upstream of the icefall~~ at an elevation of 2380 m ~~. The~~ where the thickness at the center flow line ~~of this area~~ is about 230 - 250 m and the bedrock forms an over-deepening where most of the boreholes are located ~~, see~~ (Figure 1a and Table 1~~. The average surface speed at this location is about 47 m a⁻¹ (Vincent et al., 2022).~~

~~Drilling operations took place between the 12th and the 14th September, 2019.~~). We used a custom-built hot water drill operating at 70°C to drill 10 cm diameter boreholes at an average speed of 60 m/h. ~~Insufficient weight of the driller head, fast drilling speeds, and intraglacial debris affected the verticality of the boreholes. In several occasions, probably due to the presence of rocks inside the glacier (Hantz and Lliboutry, 1983), the driller head would stop advancing, enlarging the size of the borehole at the location until drilling could be resumed. On a few occasions we could not pursue drilling and a new location had to be chosen. There were instances of sudden borehole drainage, indicating that the borehole was connected with a water pathway or a crevasse.~~ The position of the final completed and instrumented boreholes (BH1, BH2, BH3, BH4, BH5) are given by the blue dots in Figure 1a. ~~We estimate the initial shape of the boreholes calculated from the tilt and azimuth data approximately one month after installation to correct for borehole and sensor depth errors due to boreholes not being perfectly vertical (Figure 1b). Note that the actual shapes are 3D curves, so we instead show the estimated horizontal distance between each inclinometer and a vertical line starting at the surface.~~

~~**Borehole Tiltmeters (nb) Borehole depth (m) Instrumented depth (m) Bedrock depth (m)** BH1 18 208 190 253±10 BH2 19 238 234 237±20 BH3 17 216 174 235±20 BH4 19 237 211 234±20 BH5 17 194 190 234±10 Summary of the boreholes instrumentation and depths after installation. The instrumented depth refers to the depth of the last sensor. The bedrock depth is the one previously estimated by ground penetrating radar measurements (Rabatel et al., 2018; Sergeant et al., 2020)~~

The deformation rate sensors, which we refer to as tiltmeters, consist of a ~~custom printed circuit board (PCB) equipped with a~~ high-end triaxial gravity sensor (Muratta SCL3000) and a triaxial magnetic sensor (STMicroelectronics LSM303). The ~~sensors are each connected to a microcontroller (Atmega 328P) via a Serial Peripheral Interface (SPI) and Inter-Integrated~~
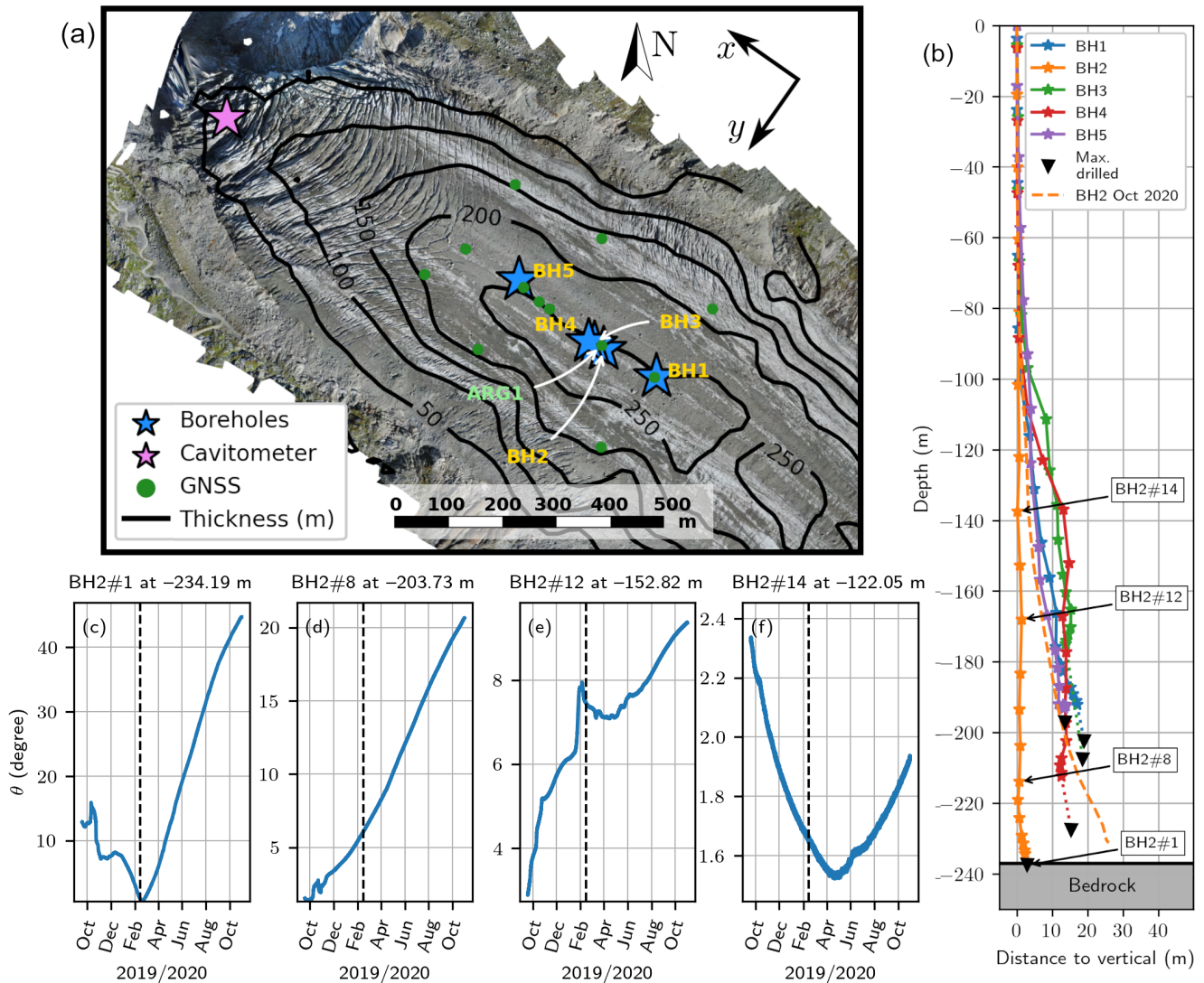
Figure 1. (a) Map of the ablation area of the Argentière Glacier (projection EPSG:27572) with ice thickness (black contours) and instrument locations. (b) Estimated initial shape, drilled depth (black triangles) and instrumented depth (every star is a tiltmeter) of the five boreholes. The dashed orange line shows the estimated shape of BH2 at the end of the tilt record. (c) to (f) Tilt θ (continuous lines) recorded at four example inclinometers in BH2 (numbers are shown on panel (b)). The dashed vertical lines mark the 15th of February 2020, the day when we start starting date of our analysis when all sensor in BH2 stabilized.

Circuit (I2C) bus, and then soldered to the PCB. PCB manufacturing and component soldering were outsourced, before each microcontroller was programmed and calibrated in the laboratory. To withstand the pressure of moving ice and water pressure, the PCB was encapsulated with an epoxy compound inside an aluminum tube with an outer diameter of 25 mm, which we call

Borehole	Tiltmeters (nb)	Borehole depth (m)	Instrumented depth (m)	Bedrock depth (m)
BH1	18	208	190	253±10
BH2	19	238	234	237±20
BH3	17	216	174	235±20
BH4	19	237	211	234±20
BH5	17	194	190	234±10

Table 1. Summary of the boreholes instrumentation and depths after installation. The instrumented depth refers to the depth of the last sensor. The bedrock depth is the one previously estimated by ground penetrating radar measurements (Rabatel et al., 2018; Sergeant et al., 2020)

the tiltmeter. The sensors are connected to a surface unit consisting of a Campbell Scientific data logger (CR300), two 12V 55Ah gel batteries and a solar panel, which allows autonomous data acquisition. Communication between the inclinometers and the surface unit is via the Modbus communication protocol over half-duplex RS485 serial buses. The gravity sensors are used to determine the position of the sensor with respect to its own reference system, from which we can derive the tilt θ, the angle with respect to the vertical, with an estimated accuracy of $0.01°$. The lab calibration has shown that tilt readings above $45°$ become increasingly unreliable. The magnetic sensors do not provide good absolute measures of orientation relative to North because they are very sensitive to parasitic magnetic fields. For this reason, we decide not to use them except to roughly estimate the initial shapes of the holes (Figure 1b).

The tiltmeters are grouped in chains of 20, more densely concentrated towards the bottom of the glacier , see (Figure 1b). For each borehole i, we name each tiltmeter j as BHi#j, starting with 1 for the deepest tiltmeter, i.e. BH2#5 is the fifth deepest tiltmeter installed in the second borehole. All sensors acquired data every 30 minutes but high frequency noise has been removed from the data by smoothing with an exponential filter with a one-day time window.

We estimate the initial shape of the boreholes from the tilt and azimuth data as averaged over the first month of record (15th of September to 15th of October 2019). The estimated shape is used to correct for borehole and sensor depth errors due to boreholes not being perfectly vertical. Although the actual shapes are 3D, uncertainties in azimuth measurements lead us to restrict our analysis of borehole shape to the estimate horizontal distance between each inclinometer and a vertical line starting at the surface (Figure 1b). In Figure 1b we also show the final shape reached by borehole BH2 before the chain of tiltmeters broke in October 2020.

Tiltmeter array performance varied between boreholes. The sensor array across boreholes. Sensor arrays in BH1 and BH5 stopped working after a few days and provided no useful data. In BH2, BH3 and BH4, all sensors recorded data for more than a year until late October 2020, when the cable snapped at an estimated depth of 220 meters, losing the deepest 6 meters. BH3 and BH4 were drilled close to BH2, with BH3 being the shortest hole of the entire campaign. Both 2020. However, both BH3 and BH4 show a very crooked tortuous shape in their deepest tiltmeters deeper sections, suggesting problems during drilling that affect subsequently affected the quality of the measurements, either by having non-vertical tiltmeters that are then too sensitive to normal strain (Keller and Blatter, 2012), or by having poor sensor-ice mechanical coupling as a result of too wide

~~borehole diameter. All sensors in BH3 and BH4 worked until November 2020. The sensors in BH5 stopped working soon after~~ ~~installation. The number of tiltmeters installed in each borehole depends on the borehole depth~~. We provide a summary of borehole and sensor corrected depths in Table 1. ~~The bedrock depth at BH2, BH3 and BH4 is based on Sergeant et al. (2020), which suggests that the DEM derived ice thickness in the vicinity of BH4 (Rabatel et al., 2018) is underestimated by about 20 m.~~ Since BH2 reaches the bed and shows good data quality, which we attribute to the nearly vertical shape of the borehole, most of the results presented in this paper are inferred solely from BH2.

~~Deformation~~ The tilt timeseries of each sensor of the three boreholes BH2, BH3 and BH4 can be found in Supporting Information S1. Tilt data during the first few months are affected by insufficient mechanical coupling between the tiltmeters and the ice ~~. We illustrate this with some representative unfiltered tilt curves in panels (c) to (f) of~~ resulting in unstable signals, up to a certain time when steady tilt occurs, which we interpret as the time when tilt meters become well coupled to the ice (Figure 1 ~~. Most sensors show an early period of noisy signals due to poor coupling to the ice, followed by a much longer period of stable tilt evolution~~c to 1f). The time ~~at which~~ of the transition between ~~noisy~~ unstable and steady tilt change ~~occurs~~ varies from sensor to sensor, from about two months for deeper sensors, where borehole closure from creep is faster, to about six months for shallower sensors, where borehole closure from creep is longer. ~~Most~~ At BH2, most tiltmeters ended up being fully coupled before the 15th of February 15 ~~,~~ 2020, that is 5 months after installation (see Supporting Information S1) ~~, when we~~. We thus start our analysis at this time. Certain sensors ~~, like BH2#1 or BH2#14, attained their~~ attained a minimum tilt after ~~September 2019, indicating they were initially tilting against the flow. Others, like~~ installation, either just after installation (e.g. BH2#8 ~~, reached their minimum tilt at, or just after, installation. Other sensors, such as BH2#12, show more erratic behavior over a longer period of time. Note the difference in tilt magnitude at different depths in Figure 1:~~) or long after (e.g. BH2#1 ~~has a total tilt change of about 60°, or~~ or BH2# ~~8 of about 25°, while BH#14's tilt change is less than 5°. We removed high frequency noise by smoothing the tilt data with an exponential filter with a one-day time window. This filtering mainly affects short-term observations and has a negligible effect on long-term (i.e. weekly or monthly averages) analysis. The tilt timeseries of each sensor of the three boreholes BH2, BH3 and BH4 can be found in Supporting Information S1~~, minimum in September 2019), indicating they were initially tilting against the flow.

2.3 Surface motion instrumentation

Five Global ~~Positioning System (GPS~~ Navigation Satellite System (GNSS) stations were deployed in the ablation zone of the Argentière glacier in February 2019, with an additional seven ~~stations~~ installed in February 2020. ~~This GPS network (green dots in Figure 1) covers the borehole sites, with station ARG1 as close as 29 m to BH2. The GPS antennas are mounted on aluminum poles anchored up to 6 m deep in the ice. The distance between neighboring survey stations ranges from 50 to 200 m. Regular field visits (monthly at most) ensure the upright position of the antenna poles and continuous power supply.~~ We employ multi-frequency Leica GR25 receivers and Leica AS10 antennas, which continuously record ~~GPS~~ GNSS signals at a 1 Hz sampling interval. ~~The raw GPS data is decimated to 30-second intervals and converted into 24-hour-long RINEX (Receiver INdependent EXchange) format files. These files~~ This GNSS receiver network (green dots in Figure 1) covers the borehole sites, with station ARG1 located ∼30 m from BH2. See also Togaibekov et al. (2024) for more details.

3 Methods

3.1 GNSS processing

GNSS signals are processed using a static approach with a double difference processing technique and ionosphere-free linear combination ~~(LC)~~ phase observables (Bock et al., 1986), incorporated in the ~~high-precision geodetic~~ software package GAMIT/GLOBK (Herring et al., 2018). ~~This strategy effectively eliminates phase biases from satellite and receiver clocks. In our static processing, we calculate a single position over 24 hours of data, although the Argentière glacier moves by more than 10 cm per day. This methodology cumulates all available satellite data whose number is reduced due to the deep valley situation of the network. It determines the position over the processing period that explains best all of the observations while averaging out multi-path interference. Daily~~ GNSS daily position time series are then converted into horizontal velocity ~~time series by subtracting successive positions over a 24 hours interval and dividing by the one-day time interval. In case the time interval of two successive positions is longer than one day (due to data gaps from missing measurements or removed outliers), no velocity is calculated. This avoids biased velocity estimates integrating position offsets unrelated to the glacier motion (e.g. re-installation of the antenna mast)~~ that are used in this study. We empirically determined a velocity error of 0.9 m/yr using a stationary ~~GPS~~ GNSS station located on the bedrock approximately 500 meters away from the survey network, which is exposed to a similar multi-path scattering environment as the stations on the glacier.

4 ~~Methods~~

3.1 Calculating internal deformation rates from tilt-meter observations

We use a three dimensional reference system with x the main along flow direction, and z the upwards vertical with origin at the surface (see panels (a) and (b) of Figure 1). Velocities in x, y and z directions are denoted by u, v and w, respectively. Assuming that the temporal evolution of the tilt θ occurs entirely in the along flow direction, the changes in θ are controlled by the horizontal shear strain du/dz and the compressive/extensive strain du/dx and dw/dz (Keller and Blatter, 2012). To detect the potential effect of compressive/extensive strain, we fit the tilt curve recorded in BH2 at each inclinometer with the ~~Keller and Blatter (2012) analytical model~~ analytical model of Keller and Blatter (2012) (see Supporting Information S2). We find that ~~the best fit with the data~~ best data fit can always be obtained by neglecting du/dx and dw/dz apart for the two deepest sensors (BH2#1 and BH2#2) where a better fit is obtained with non-zero compressive strain. ~~Indeed, neglecting here the compressive strain would lead~~ For these deepest sensors, neglecting compressive strain leads to an overestimation of du/dz by about 30% ~~and 20% at the sensor~~ at BH2#1 and 20% at BH2~~#2 respectively.~~ 2. The presence of significant compressive strain near the glacier bed is likely related to a local effect of bed roughness ~~that is negligible elsewhere, which is confirmed by the numerical model (see Section 4.2). This is also consistent with the~~ as shown by the local evaluation of strain over a rough bed done in Section 5.1~~, which suggests that the tilt curves are significantly affected by horizontal compressive/extensive strain du/dx below 220 m depth in a layer we will refer to hereafter as the~~ . Hereafter we refer to this layer as the basal boundary

layer. ~~The~~ Therein the derived du/dz ~~in this layer are therefore likely~~ values are expected to be strongly biased and ~~will be~~ are thus ignored in the ice rheology interpretation.

With the hypothesis that du/dz dominates the flow gradient outside of the boundary layer, the internal deformation rate du/dz from the temporal evolution of the tilt θ is computed as (Lüthi et al., 2002; Ryser et al., 2014; Doyle et al., 2018; Maier et al., 2019),

$$\frac{du}{dz} = \frac{1}{dt}\frac{dx}{dz} \approx \frac{1}{\Delta t}\Delta \tan(\theta), \tag{1}$$

where Δt is a given time period and $\Delta \tan(\theta)$ is the change in the tangent of tilt during that time period. In our particular implementation, we calculate the least squares linear approximation of $\tan(\theta)$ as a function of time during each Δt period (set to one day), such that the regression coefficient ~~gives directly~~ directly gives du/dz. The estimated maximum uncertainty for the daily averaged deformation rate is, for most of the sensors, lower than 0.1 a^{-1} ~~, more details can be found in the~~ (see Supporting Information S3).

3.2 Computation of surface, internal and basal velocities timeseries

As it is not always possible to directly interpolate surface velocity at the borehole location from the ~~GPS network~~ GNSS network due to data gaps, we construct a continuous timeseries of the surface velocity at the ~~GPS~~ GNSS station close to the boreholes by filling gaps using a linear model traditionally used to construct continuous surface mass balances from sparse data on alpine glaciers (Lliboutry, 1974; Vincent et al., 2017). In this linear model we assume similar temporal variability in surface velocity across stations, such that surface velocity at each ~~GPS~~ GNSS station i can be expressed as

$$u_{si}(t) = \alpha_i + \beta(t), \tag{2}$$

with α_i the average surface velocity at the station i over ~~2020~~ the measurement period, and $\beta(t)$ the temporal variability assumed identical for all stations and satisfying $\sum \beta(t) = 0$. We first solve for the system of equations by finding the values of α_i and $\beta(t)$ that best approximate the observations while ~~keeping~~ satisfying $\sum \beta(t) = 0$. We then compute the residuals between modeled and observed ~~velocity~~ velocities and their standard deviation s_{res}, and classify as outliers all observations with residuals greater than $3s_{res}$. We finally solve for the system again without these outliers to obtain the final values of α_i and $\beta(t)$. The residuals ~~of the~~ between observed and reconstructed velocities follow a normal distribution centered ~~close to~~ around 0 ~~which validate~~, which validates the initial assumption (Supporting Information S4). The surface velocity timeseries $u_s = \alpha_{ARG1} + \beta(t)$ (s_{res} = 3.2 m a^{-1}) is thus used to fill the gaps at the ARG1 station, which lies the closest to BH2 as seen in Figure 1.

The internal velocities are computed by integrating the deformation rate over depth,

$$u_d(z,t) = \int_{z_{bed}}^{z} \frac{du}{dz}(z,t)dz \tag{3}$$

where z_{bed} is the bedrock elevation (m). Finally, the basal velocity $u_b(t)$ is computed as the difference between the reconstructed surface velocity $u_s(t)$ and the integrated deformation rate over the whole ice thickness $u_d(t)$. The timeseries are

computed at a daily resolution from the daily averaged deformation rate. ~~We also compute the daily average of the sliding velocity at the cavitometer with a precision of about 3.5 m a-1 and the subglacial discharge with a threshold of approximately 10 m3 s-1 (Vincent and Moreau, 2016).~~

3.3 Quantifying Glen's flow law parameters

~~Assessing the~~ In addition to deformation measurements, the study of ice rheology requires ~~confronting the deformation measurements to the stress tensor τ_{ij} that need to be evaluated~~ knowledge of the stress field within the ice, which is evaluated in this study using numerical modelling. We use the three-dimensional full-Stokes finite-element model Elmer/Ice (Gagliardini et al., 2013) to solve for conservation of momentum equation under a given glacier geometry and ice rheology. The glacier geometry is prescribed based on measured bedrock topography and surface topography derived from Pleiades satellite imagery on August 25, 2019 (Beraud et al., 2022). The ice rheology is given by Glen's flow law:

$$\dot{\varepsilon}_{ij} = A\tau_e^{n-1}\tau_{ij}, \tag{4}$$

where $\dot{\varepsilon}_{ij}$ and τ_{ij} are respectively the components of the strain rate (a^{-1}) and deviatoric stress (MPa) tensors, A is the creep factor ($MPa^{-n}\ a^{-1}$), $\tau_e = \sqrt{\frac{1}{2}\tau_{ij}\tau_{ij}}$ is the effective stress (MPa) and n ~~the Glen's~~ is an exponent. We assume a stress-free upper surface boundary condition and a basal boundary condition ~~given by a~~ as given by the Weertman friction law (Weertman, 1957),

$$A_s\tau_b^m = u_b, \tag{5}$$

where τ_b is the basal shear stress (MPa), m ~~an exponent taken equal to~~ is an exponent setting the non-linearity of the law and is taken be 3 (Gilbert et al., 2023), A_s is the sliding coefficient at the bed ($m\ a^{-1}\ MPa^{-m}$), and u_b is the sliding velocity ($m\ a^{-1}$). We use values of A_s for ~~m~~ m=3 ~~taken from Gilbert et al. (2023) inferred~~ as inferred in Gilbert et al. (2023) from surface velocity inversion. To avoid stress anomaly produced by uncertainty in the ice thickness, we relax the surface topography for 1 year, using surface mass balance forcing from Gilbert et al. (2023), before extracting the deformation rate and stress tensor from the model.

We run several simulations to test the sensitivity of the deformation rate profile to different values of A and n. We run a set of simulations with $n = 3, 4, 5$ and constant and uniform creep factor A. The value of A for each n is chosen such that the numerically calculated total deformation velocity at the location of BH2 matches the ~~observations~~ observed one. To minimize the potential effect of temporal changes in basal friction on the stress field (Hooke et al., 1992; Willis et al., 2003), we use the averaged deformation rate profile recorded during the last month of the timeseries (1st to 31st of October 2020) when the basal friction is the least affected by subglacial hydrology and the inclinometers are well coupled to the ice. We run another set of ~~simulation with~~ simulations using $n = 3$ and a depth-dependent creep factor $A = A(z)$ such that the computed ~~deformation rate du/dz match the observations. To find the creep factor as a function of depth, we infer A by~~ profile matches that observed. We infer $A(z)$ using Glen's ~~law (Eqn~~ flow law (Eq. (4)) knowing the observed mean du/dz at BH2 and the stress tensor computed from the Elmer/Ice simulation such that
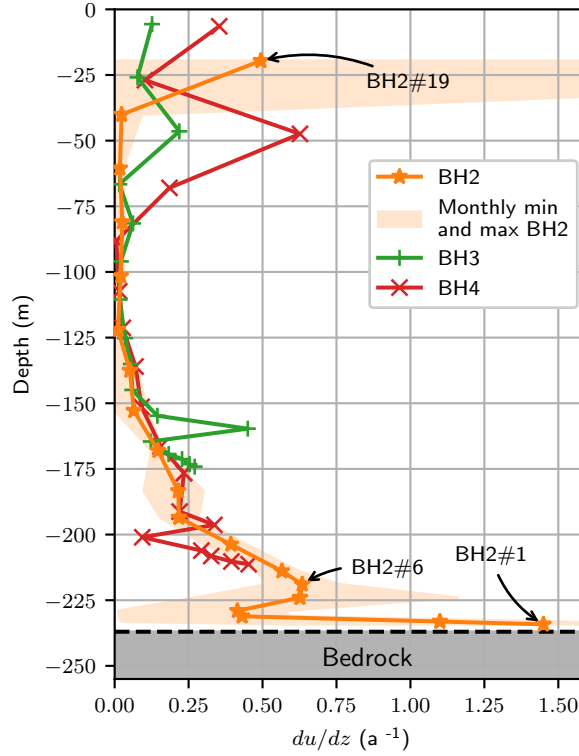
Figure 2. Average measured deformation rate profiles with monthly minima and maxima at BH2, BH3 and BH4 including the monthly minima and maxima for BH2. The continuous lines show the average measured deformation rate profile at each borehole for the period between the 15th February and the 15th of October 2020, and the shadowed region the range between monthly averaged minima and maxima deformation rate values (shown only for BH2). Every symbol represents a tiltmeter.

$$A(z) = \frac{1}{2} \frac{du}{dz} \tau_{E,num}^{-2} \tau_{xz,num}^{-1}. \tag{6}$$

We then approximate $A(z)$ by a piece wise linear function $A_{fit}(z)$ ~~to obtain a depth-dependent viscosity~~. Given that changing the creep factor slightly modifies the overall stress balance, we run the numerical model repeatedly, updating at each iteration the $A_{fit}(z)$ inferred with the numerical solution of the previous iteration, until the modeled stress field converges. The depth-dependent creep factor ~~A(z)~~ $A_{fit}(z)$ determined at BH2 is applied uniformly over the entire domain by normalizing it with depth and applying this normalization everywhere.
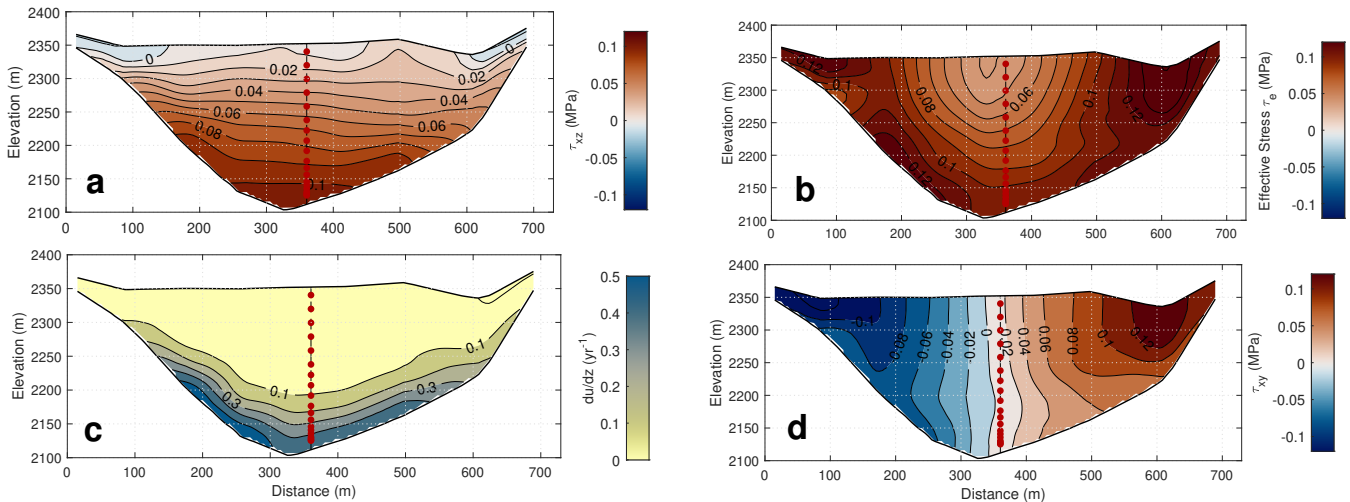
Figure 3. Modeled shear stress τ_{xz} (a), effective stress τ_e (b), deformation rate du/dz (c) and shear stress τ_{xy} (d) along a transversal cross section at BH2 location. The inclinometers from BH2 are shown as red dots.

4 Results

4.1 Observed mean deformation rate profiles

In Figure 2 we show the average deformation rate profiles computed from tilt measurements (see methods in Section 3.1) at BH2, BH3, and BH4 ~~and averaged between the 15th February and the 15th October 2020 are shown in Figure 2.~~ between 15 of February and 15 of October 2020. The orange shaded region shows the range associated with monthly-averaged deformation rate du/dz for BH2. The retrieved profiles show similar depth-increasing deformation rate ~~, but only~~ with only few outliers associated with the high deformation rate at ~-160 m in BH3 and the low deformation rate at ~-200 m in BH4. These outliers are likely measurement artefacts as noticeable in the raw data (see Supporting Information S1, BH3#6 and BH4#5). Only BH2 reached the bed (see Figure 1b and Table 1) ~~. BH2~~ and also shows generally lower measurement noise likely due to better ice coupling (see Supporting Information S1). For both of these reasons, from now on we focus on the deformation rate profile recorded at BH2 only, which we divide in three parts.

The upper part (uppermost 120 m) of the deformation rate profile ~~, spanning the uppermost 120 m,~~ of BH2 has a small shear deformation rate ($\approx 0.02 \, a^{-1}$) ~~.~~ except BH2#19, which shows very noisy records and is thus disregarded from our analysis (see Supporting Information S1). The middle part, from -120 m until -219 m (BH2#6), is characterised by much higher deformation rates increasing non-linearly towards the bed, from less than 0.02 a⁻¹ at -120 m to a local maximum of 0.63 a⁻¹ at -219 m. Below -219 m starts the ~~lowest part, which~~ section we refer to as the boundary layer ~~. This part~~, which includes a 40% decrease in deformation rates over the first 10 meters below -219 m, followed by a more than threefold increase in du/dz ~~between~~ from -230 m ~~and~~ to -235 m, ~~up to almost~~ where deformation rate reaches a maximum of 1.5 a⁻¹ ~~near the bed at -235 m, which corresponds to the highest deformation rate of the profile.~~
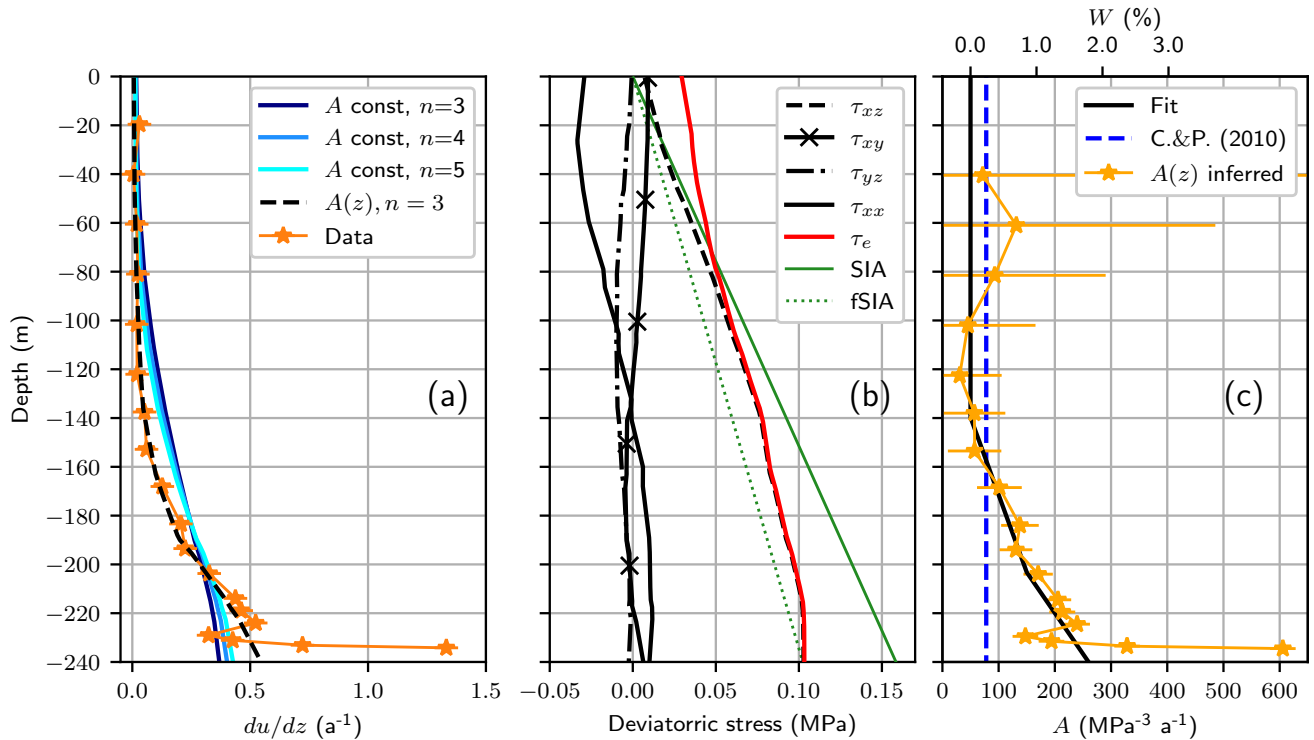
Figure 4. (a) Observed and modeled deformation profile at BH2 with uniform creep factor and $n = 3$, $n = 4$, and $n = 5$, and with depth-variable creep factor $A = A(z)$ and $n = 3$. (b) Vertical profile of different modeled stress components (compressive is negative). The Shallow Ice Approximation (SIA) solution without shape factor is given for comparison (green dotted line). (c) Inferred creep factor using measured deformation rate and modeled effective stress at BH2 from Eq. (6) (bottom horizontal axis). The corresponding water content according to Duval (1977) is shown by the top horizontal axis. The blue dashed line marks the value of A proposed by Cuffey and Paterson (2010).

4.2 Ice flow model

Ice flow ~~at the BH2 site is found to be~~ as predicted by our model is mainly dominated by along flow shear τ_{xz} and lateral shear τ_{xy} (Figure 3). ~~The lateral shear can reach significant values away of the central line and greatly affect~~ Lateral shear is
310 significant on the side of the glacier where it greatly affects the effective stress τ_e and thus ~~deformation rate on the side of the glacier~~ the deformation rate (Figure 3). However, in the center line around BH2, the magnitude of τ_{xy} ~~remains very small compared to the shear along the~~ is very small (<0.02 MPa) compared to that of shear along flow τ_{xz} ~~at the drilling site~~(>0.08 MPa where most deformation occurs), making our measurement ~~principally~~ mainly influenced by τ_{xz}. ~~Other~~ We find that other components of the stress tensor ~~have been found to be~~ are small compared to τ_{xz} (<10%), except near the surface where they
315 can be of similar amplitude (see Supporting Information S5). Modeled flow gradient tensor components du/dx and dw/dz are very small (see Supporting Information S5) which ~~validates~~ suggests the use of Eq. (1) to calculate du/dz is appropriate (see

Section 3.1). We also find that the stress tensor is rather insensitive to the choice of rheological parameters and is mainly controlled by the glacier geometry (Supporting Information S5). Comparing our result with a simplified plane-strain model, commonly referred to as the Shallow Ice Approximation (SIA), we show that shear stress as estimated using SIA is overestimated (see Figure 4b), leading to an incorrect quantification of the rheological parameters. Following Nye (1965), use of a shape factor $f = 0.646$ in the SIA formulation would account for the effect of the parabolic valley shape (considering a half-width to thickness ratio of 2, a reasonable approximation of the Argentière glacier cross-section at the study site, see Supporting Information S6). Applying this correction improves the stress representation obtained using the SIA, but large discrepancies remain (see Figure 4b, green dotted line), with the corrected SIA underestimating the effective stress all along the profile except at the bottom, where the basal shear stress matches that of the full Stokes model.

We find that simulations with constant creep factor A and varying Glen's law exponent $n = 3, 4, 5$ yield deformation rate profiles exhibiting much lower non-linearity with depth than observed (see Figure 4a). The use of a constant creep factor thus does not allow explaining the observed profile, regardless of the value of n which turns out to be poorly constrained in this context as a result of stresses not varying strongly with depth (Figure 4b) . To be consistent with the commonly used value of n and infer a relevant creep factor for ice flow modeling in general, we thus assume $n = 3$ and quantify A following the method described in Section 3.1 (Figure 4c).

Using the linear piece wise approximation of A (black line in Figure 4c), the simulation provides a good match with observations (Figure 4a), apart from the deformation rates recovered in the boundary layer, which are poorly reproduced by the numerical model. This discrepancy is likely due to bed topography being too low resolution to capture stress variations nearby unresolved local bed irregularities, and also because our observed du/dz values may be strongly biased due to compressive/extensive strains being neglected in the present analysis while likely significant within the boundary layer (see Section 3.1). For that reason, we consider that the values of A inferred in the boundary layer are not relevant. In Figure 4c, we see that the inferred creep factor $A(z)$ in the upper half of the glacier is compatible with the value proposed by Cuffey and Paterson (2010) for temperate ice, but increases by up to a factor ~ 4 from -140 m down to the top of the boundary layer (-219 m) . We discuss this depth-increasing creep factor in Section 5.2.
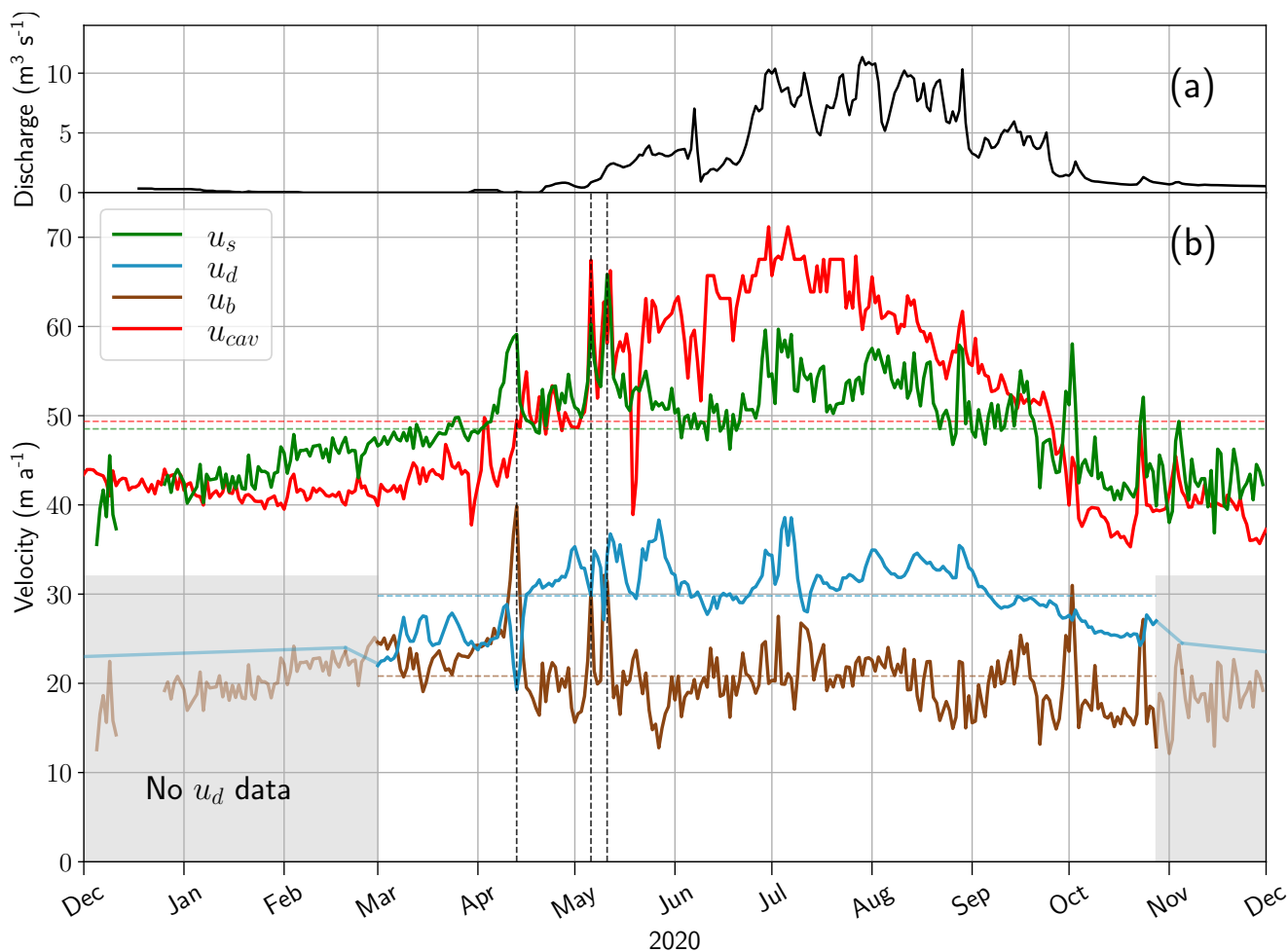
Figure 5. ~~Daily~~ Computed timeseries of daily subglacial discharge (a) and velocities (b) at the Argentière Glacier. The panel (b) shows the surface velocity computed with the linear model for the ~~GPS~~ GNSS station ARG1 u_s, the deformation velocity at BH2 u_d, the inferred basal velocity at BH2 u_b and the sliding velocity at the cavitometer u_{cav}. The horizontal dashed lines correspond to the average velocities over the studied period. In the shaded area, an estimation of the sliding velocity (~~black~~ brown line) is shown assuming a linear trend in the deformation velocity (blue line). The vertical dashed line show speed up events that are referred to in the text.

4.3   ~~Seasonal~~ Temporal evolution of ~~velocity~~velocities

On the seasonal timescale, the surface velocity shows an annual cycle with a gradual increase between December and May, a period of stagnation until mid-September and a decrease until December (Figure 5). The period of stagnation coincides with the melting period as shown by the observed high discharges. Surprisingly, however, the deformation velocity also shows a seasonal variation~~with~~, with a similar phase and amplitude to that of surface velocity~~, suggesting that the~~. As a result, basal velocity remains roughly constant throughout the year. This is in contrast to in-situ observations of basal velocity at

the cavitometer, where sliding velocities show a strong seasonal variability materialized by highest sliding speeds in July and lowest in February/March (Figure 5b, see also Gimbert et al. (2021a)). These results are further discussed in Section 5.3.

On shorter timescales, the relationships between surface, deformation, and sliding velocities are different from those observed at the seasonal timescale. Peaks in surface velocity that occur at the beginning of the melt season (Togaibekov et al., 2024) coincide with a decrease in deformation velocity and a strong increase in sliding velocity (see highlighted as vertical dashed lines in Figure 5). These peaks are also visible at the cavitometer, particularly for the May events. At the end of the melt season (October), peaks of surface velocities are also mainly explained by changes in sliding speed but do not necessarily coincide with a decrease in deformation velocity as observed for the early melt season peaks.

To better understand the origin of temporal changes in the deformation velocities, we investigate to which extent these occur in proportion to changes in du/dz with depth. For that we define s_n as the standard deviation of the monthly averaged values of du/dz normalized by du/dz as averaged between 15th of February and 15th of October 2020. We show that s_n is consistently on the order of 20% with no preferential localisation in a specific section of the ice column (Figure 6b). A more detailed analysis of du/dz variations at each sensor shows that most of them exhibit a similar seasonal cycle with maximum deformation in summer (see Supplementary Information S7). Temporal variations of du/dz at any given depth thus generally occur in proportion to the long term du/dz average value. Only four sensors (BH2#6,11,12,14) significantly depart from this general picture, either through exhibiting a different phasing (#6,12,14) or a different amplitude (#11) (Figure S17) which may be due to poor coupling with the ice (the noise level for #12 and #14 is particularly high.

5 Discussion

5.1 Identification and interpretation of the boundary layer

The shape of the deformation rate profile and the retrieved values of du/dz close to the bed suggest intense deformation due to local stress concentrations around bedrock irregularities within the boundary layer (Maier et al., 2019). We qualitatively explored the viability of this explanation with a simulation of tilt evolution close to the bed using the deformation rates provided by Gudmundsson (1997) and the model of tilt evolution in a given velocity field provided in Gudmundsson et al. (1999), which we explain in the Supporting Information S8. In Figure S18, we show that significant compressive or extensive horizontal strain-rates du/dx localise close to the bed and dominate the flow gradient in a boundary layer with a thickness equal to ~ 6 times the vertical amplitude of the bedrock bump. We find that under the hypothesis of Eq. (1) and using synthetic tilt timeseries produced from the
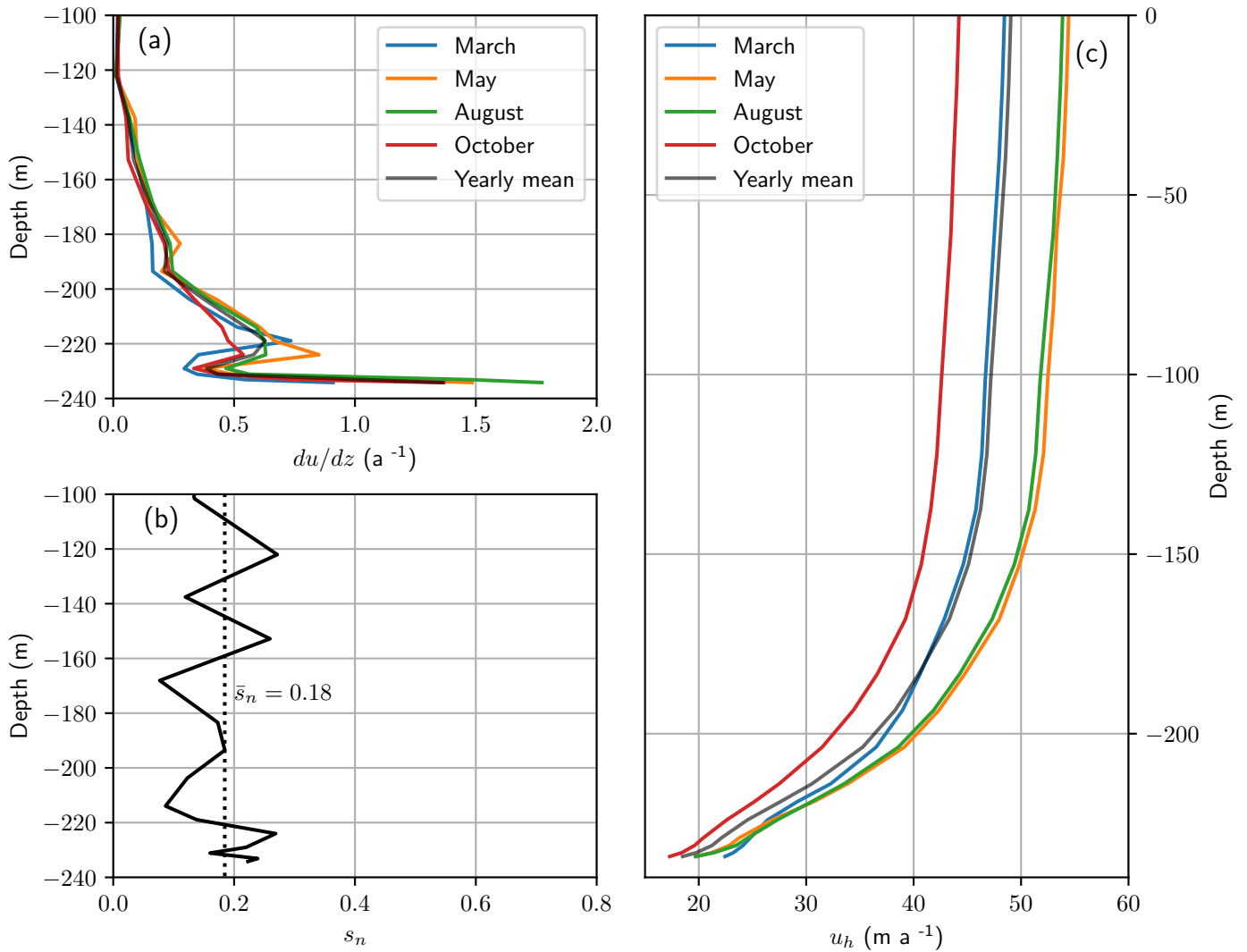
Figure 6. (a) Monthly and yearly du/dz profile at four periods (see legend). (b) Standard deviation of the monthly averaged du/dz profile normalized by the du/dz averaged between 15th February and 15th of October 2020. (c) Monthly and yearly horizontal velocity u_h profile at four periods (see legend).

estimated strain-rates, the inferred apparent du/dz would have a zigzag shape similar to ~~the one~~ that observed in Figure 2.

390   This suggests that the zigzag shape in the ~~data~~ reconstructed du/dz is an artifact resulting from neglecting du/dx and not a real variation in du/dz. The comparison between our reconstructed du/dz from the tilt data and the inferred apparent du/dz using Gudmundsson (1997) and Gudmundsson et al. (1999) models suggest that ~~the drill reach~~ we drilled on the summit of a ~~bed rock bump of $\approx$ 2 m~~ bedrock bump of ~ 2 m vertical amplitude.

~~Study Glacier Area Avg. *W* (%) Method Notes Joubert (1963) Accum. 0.15 - 0.1 Calorimeter Lliboutry (1971) Calorimeter Vallon et al. (1976) Accum. 0.32 - 1.31 Calorimeter Zryd (1991) - 0.5 — 1.5 Calorimeter Basal ice Cohen (2000) - Calorimeter Basal iceMurray et al. (2000) Ablat. 0 - 3.3 GPR Benjumea et al. (2003) Accum. 0.6 - 2.3 GPR and seismics Hubbard et al. (2003) Both Ion concentration Murray et al. (2007) Ablat. 1.18 - 3.8 GPR Ablat. 2 Calorimeter Basal ice~~
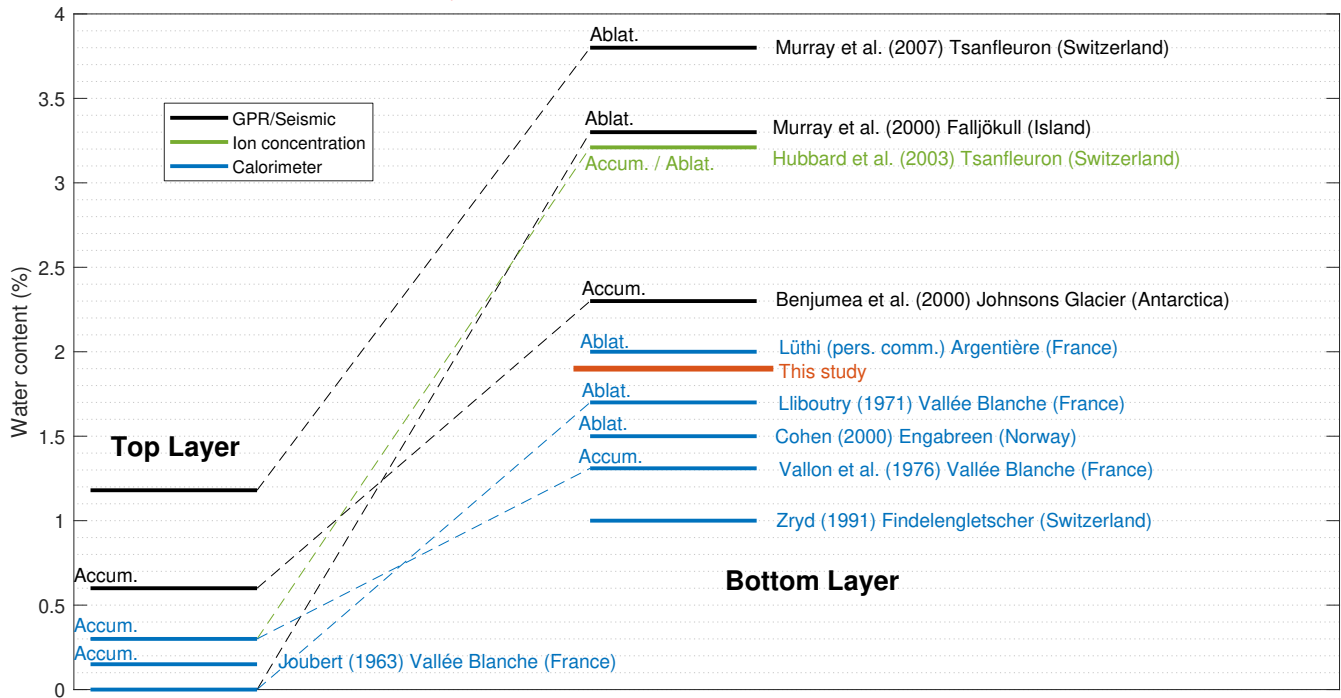
Figure 7. Synthesis of water content measurements made in temperate glaciers ~~, with~~ ~~emphasis on~~ distinction between the ~~studied area of~~ top layer (close to the ~~glacier~~ surface) and the ~~in-depth distribution~~bottom layer (close to the bedrock). The color indicate the methods (GPR/Seismic, Calorimeter, Ion concentration). We use the abbreviation ablat. to refer to the ablation zone and accum. to refer to the accumulation zone.

5.2 Interpretation of the depth-increasing creep factor

395 ~~Since~~ Argentière Glacier is fully temperate, ~~depth-increase of the creep factor may be due to an increase in interstitial water content *W* with depth (Duval, 1977; Adams et al., 2021)~~i.e. ice lies at the pressure melting point through the entire ice column, such that the observed increase in creep factor with depth must result from factors other than changing temperature. We test ~~this hypothesis using the formula proposed by (Duval, 1977) to convert the estimated~~ the hypothesis that the depth-increase in creep factor ~~into~~ is due to an associated increase in ~~water content~~interstitial water content W by linking these two quantities

400 using the formula proposed by (Duval, 1977). Adapting the formulation from Duval (1977) by considering $A = 50$ MPa^{-3} a^{-1} when $W = 0$ as a reference value, i.e., assuming no water content in the upper half of the glacier, we obtain

$$W = \frac{1}{2.34}\left(\frac{A}{50} - 1\right), \qquad\qquad (7)$$

with W in % and A in MPa^{-3} a^{-1}. The inferred water content values are given in the top horizontal axis of Figure 4c. Discarding the negative values as artifacts of our chosen ~~parameterization~~ parametrization of Duval's model, we see that the expected water content above -219 m ranges between 0 and 1.3%, increasing down to the bed. Below this depth, the deformation profile is likely influenced by enhanced stress and underestimated velocity gradients due to local basal roughness and cannot be interpreted ~~by~~ in terms of enhanced creep factor (see Section 5.1). These values of W, and this type of spatial distribution, are comparable to those observed in temperate ice (see ~~Table ??~~Figure 7). The depth-increasing creep factor is thus compatible with the effect of depth increasing water content.

Our ~~finding~~ suggestion of increased water content with depth could appear to be in contradiction with that of ~~of~~ Lliboutry and Duval (1985), who report no relationship of W with depth through analysis of an ice core obtained in the Argentière Glacier in a location close to our boreholes (Hantz and Lliboutry, 1983). However, the ~~engineers and~~ researchers that performed the measurements deem them untrustworthy as a result of water content being primarily correlated with the air temperature under which the measurements were made at the glacier surface, with higher temperatures increasing ice core melt and thus artificially ~~increased~~ increasing measured water content (Michel Vallon, ~~personnal~~personal communication). For these reasons we do not include ~~Lliboutry and Duval (1985) is not included in Table ??~~ results from Lliboutry and Duval (1985) in Figure 7 although it previously appeared in ~~well cited~~ other compilations of observations of interstitial water content (e.g. Pettersson et al., 2004; Cuffey and Paterson, 2010). We also note that the absolute values of water content as inferred using the relationship proposed by Duval (1977) may be associated with high uncertainty, since this empirical relationship was obtained in the laboratory by shearing temperate ice in tertiary creep with water contents up to 0.8% and has not been validated for higher values of water content. Recently, Adams et al. (2021) found in similar experiments that ice viscosity under secondary creep is nonsensitive to water content for $W > 0.6\%$, but we do not expect these results to apply in the present case since tertiary creep is expected under the high cumulative deformations of Argentière Glacier (Lliboutry and Duval, 1985; Budd and Jacka, 1989).

Although water content is our identified best candidate to explain the increase in creep factor with depth, we note that other factors could be at play, such as depth-decreasing grain size or changes in ice anisotropy (Cuffey and Paterson, 2010; Montagnat and Duval, 2004). ~~However, Vallon et al. (1976) reported no discernible change in grain size except at the bed in the accumulation zone of La Mer de Glace, a glacier close to the Argentière Glacier. The role of anisotropy~~ The role these factors would need to be specifically analyzed by quantifying the evolution of grain size and ice textures with depth at the measurement site in order to be able to discard or not ~~its~~their respective influence on ice viscosity.

5.3 Temporal changes in deformation velocity

We show that the deformation velocity varies seasonally by ~~≈30%~~ $\sim 30\%$ (Figure 5), which, using Glen's flow law with $n = 3$, implies either a stress change of ~~≈9%, either~~ $\sim 9\%$, or a change in the creep factor of ~~≈30%. The seasonal variability of the creep factor value could be explained by a seasonal change in water content of ≈60% uniformly~~ $\sim 30\%$, the latter of which
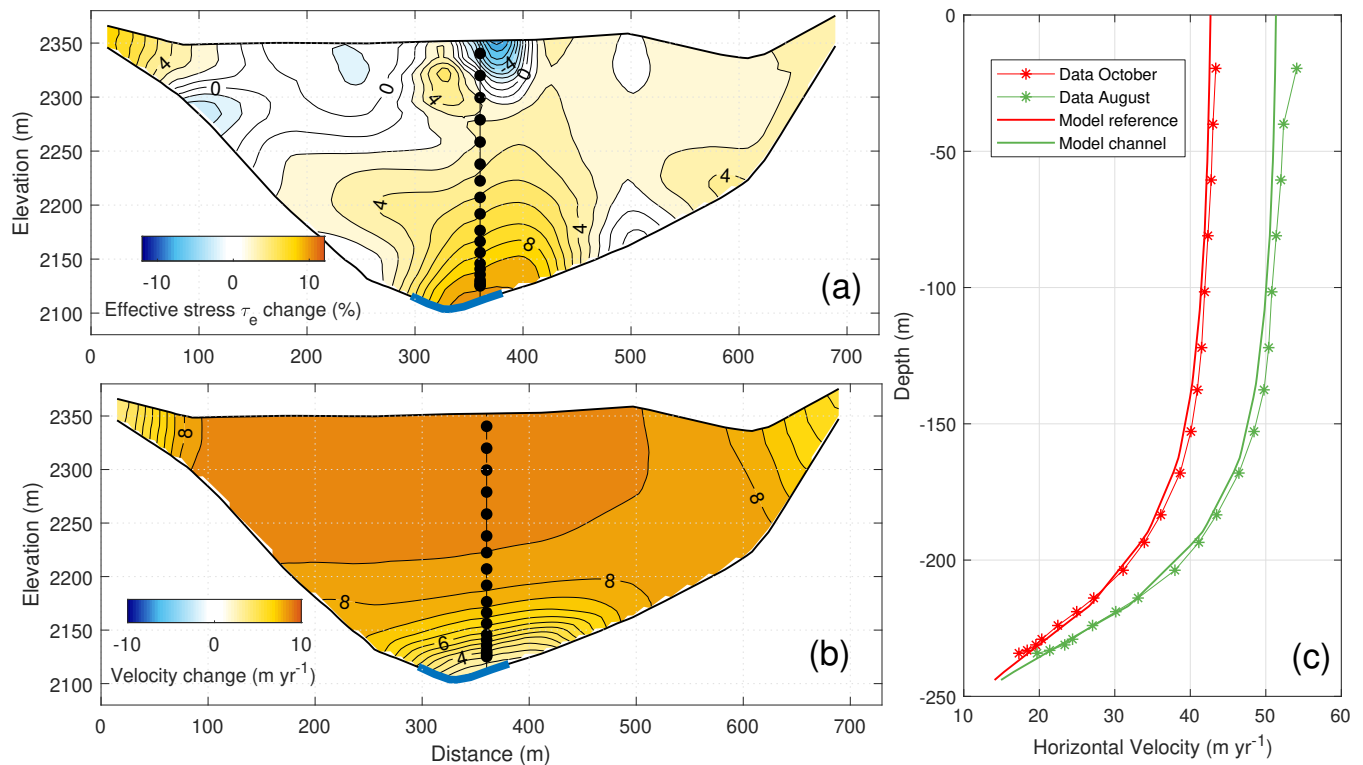
Figure 8. Modeling change in effective stress (a) and horizontal velocity (b) due to non-uniform variation of basal friction. We assume that, during melting period, friction increase in the central part (blue thick line on panels (a) and (b)) and friction decrease elsewhere due to channelized efficient drainage in the central line contrasting with inefficient cavity network elsewhere. The inclinometers of BH2 are shown as black dots in (a) and (b). Panel (c) shows modeled and observed velocity profile at BH2 in August and October.

would require the water content to be multiplied by 1.6 over the entire ice column, which seems unrealistic, since the increased

445 ice deformation in summer. Although microcracking in response to changes in surface melting and subglacial water pressure can provide significant amounts of water at depth(Gajek et al., 2021), yet the extent to which this mechanism would alter the interstitial water content at the source of ice softening remains unknown. In addition, an increase in microcracking at depth in summer is inconsistent with the observed decrease in basal water pressure. Other than from microcracking, a 30% increase in deformation heat ($\approx + 3 \times 10^{-4}$ W m^{-3}) would produce an excess of water content of only $\approx 0.17\%$ due to increased strain

440 heating. Also, the stress changes $\sim 0.17\%$ over one month (the time within which the deformation change occurs), which would have a much lower than observed effect on the creep factor. Finally, with regard to the stress variation hypothesis, a 9% stress change cannot be explained by the seasonal evolution of ice thickness, which is maximum in May and decreases until October (Vincent et al., 2022) and thus out of phase with the observed deformation rate. Furthermore, the amplitude of the thickness change at the BH2 site is about 6 m (Vincent et al., 2022), which represents only a 2% stress change.

445 The most plausible hypothesis

The hypothesis that we find most plausible to explain the seasonal variability in deformation rate observed at BH2 is through changes in stress distribution due to non-uniform spatial changes in basal drag during the melting season, as previously suggested in Hooke et al. (1992) and Willis et al. (2003). The loss of drag in response to meltwater input in areas surrounding the observation site can locally increase stress through stress transfer in the form of lateral shear. This could be caused by differences in subglacial hydrological conditions between the glacier centerline and its sides. The lack of change in basal velocity during summer at BH2 (Figure 5), while deformation velocity and stress increased, suggests that basal friction also increased in the central part of the glacier to accommodate more stress while remaining at a constant velocity. This could result from the development of efficient drainage in the central part of the glacier, as previously identified from seismic observations ~~by Nanni et al. (2021)~~(Nanni et al., 2021), which reduces water pressure and thus promotes high friction along the central line, while the sides remain dominated by higher pressure inefficient drainage promoting lower basal friction. To investigate this hypothesis, we perform a complementary numerical simulation where we increase the friction around a central ~~≈~~$\sim$50 m wide area (assumed to be affected by an efficient drainage) and decrease it elsewhere (see Figures 8a and 8b). We find that, relative to the reference state in October 2020, a decrease of 20% of A_s in the central part combined with an increase of 70% of A_s elsewhere is able to produce the stress change needed to explain the enhanced internal deformation observed in summer (Figure 8c). Such a contrast in A_s (factor 2.1) is compatible with that expected when cavitation occurs or not (Gimbert et al., 2021a; Gilbert et al., 2022; Maier et al., 2022). This view is also consistent with the findings in Vincent et al. (2022) that bed separation by cavitation increases between January and July with greater amplitude on the glacier margin than on the midline. It leads to an increase in basal sliding during this period, as observed in our data (Figures 5 and 6c). An evolving drag contrast between the center and side of the glacier would also explain why strong peaks in surface velocity are associated with a decrease in deformation velocity during the early melt season. Early water input into the not-yet-developed efficient drainage in the centerline of the glacier may lead to pressurization of the central channel, reducing drag in the centerline relative to the side of the glacier. This effect would be less pronounced in autumn because channels are still of significant size after summer, and this would explain why the decrease in deformation velocity during surface velocity peaks is not observed in autumn but only in spring (Figures 5).

6 Conclusions

Using borehole inclinometry~~techniques~~, we were able to reconstruct the deformation profile along the central line of the ablation area of Argentière Glacier and its evolution over eight months, including the entire melt season. ~~These observations allow us to quantify~~ We quantified the Glen's flow law creep factor by ~~modeling~~ combining our observations with modeling of the local stress field using a three dimensional full Stokes ice flow model, which appears to be different from what the SIA would predict, making its use inappropriate at our study site. We show that surface values (above 100 m depth) of the creep factor are consistent with the standard value for temperate ice (Cuffey and Paterson, 2010), but increase progressively below this depth up to 200 MPa^{-3} a^{-1}. We interpret the depth-increasing creep factor as an associated increase in water content from 0 to 1.3 ~~percent using Duval (1977)'s law, which is a~~ %, which are reasonable values given previous in-situ water

content measurements from the literature (~~Table ??~~Figure 7). We also find seasonally evolving deformation rates, with higher deformation rate occurring during the melt season~~. The evolution of the~~, such that the local deformation velocity explains most of the evolution of the surface velocity on a seasonal time scale. We show that ~~the seasonal variability in deformation rate at the study area~~ this variability is due to changes in stress distribution within the ice body in response to the evolving contrast in basal drag between the centerline and the rest of the glacier during the melt season. We interpret the difference in drag at the center of the glacier as the effect of efficient drainage developing at the deepest point of the subglacial valley.

This study demonstrates the significant value in using borehole inclinometry for inferring ice rheology and local changes in basal friction that cannot be detected through surface velocity observations. The data obtained provides rare insights into how subglacial hydrology, basal friction, and surface velocity are interconnected.

Code and data availability. All data used in this article and the code to process it can be accessed through the Zenodo repository available at https://zenodo.org/records/13961256

Author contributions. JP. Roldán-Blasco processed the tilt data and A. Gilbert designed and performed the numerical simulations. JP. Roldán-Blasco, A. Gilbert and F. Gimbert wrote the manuscript. L. Piard designed the tiltmeters, directed the field campaign and performed early analysis on the data. L. Piard, A. Gilbert, F. Gimbert, C. Vincent and O. Gagliardini participated in the inclinometry field campaign and together with JP. Roldán-Blasco analysed the data, while A. Togaibekov and A. Walpersdorf provided the GNSS measurements and velocity timeseries. All authors contributed to finalizing the manuscript.

Competing interests. The authors declare no competing interests.

Acknowledgements. The authors would like to thank Bruno Jourdain, Olivier Laarmann, Maël Richard and everybody else that participated in the 2019 field campaign and the fabrication of the instruments. This work is supported by the French ANR project SAUSSURE (ANR-18-CE01-0015-01, https://saussure.osug.fr). We also thank Luc Moreau for providing the cavitometer data and Electricité d'Emosson for the discharge measurements. Glacier surface elevation and precipitation data were acquired in the framework of the GLACIOCLIM program (https://glacioclim. osug.fr). OG acknowledges support from the project FricFrac funded by the Center for Advanced Study (CAS) at the Norwegian Academy of Science and Letters during academic year 2023-2024. The authors would like to thank Dominik Gräff and Manuela Köpfli for their careful reading and suggestions during the review process, which significantly improved the quality of the manuscript.

References

Adams, C. J., Iverson, N. R., Helanow, C., Zoet, L. K., and Bate, C. E.: Softening of Temperate Ice by Interstitial Water, Frontiers in Earth
505   Science, 9, 1–11, https://doi.org/10.3389/feart.2021.702761, 2021.

Amundson, J. M., Truffer, M., and Lüthi, M. P.: Time-dependent basal stress conditions beneath Black Rapids Glacier,
     Alaska, USA, inferred from measurements of ice deformation and surface motion, Journal of Glaciology, 52, 347–357,
     https://doi.org/10.3189/172756506781828593, 2006.

Arthern, R. J. and Gudmundsson, G. H.: Initialization of ice-sheet forecasts viewed as an inverse Robin problem, Journal of Glaciology, 56,
510   527–533, https://doi.org/10.3189/002214310792447699, 2010.

Barnes, P., Tabor, D., and Walker, J. C. F.: The friction and creep of polycrystalline ice, Proceedings of the Royal Society of London. A.
     Mathematical and Physical Sciences, 324, 127–155, https://doi.org/10.1098/rspa.1971.0132, 1971.

Benjumea, B., Macheret, Y. Y., Navarro, F. J., and Teixidó, T.: Estimation of water content in a temperate glacier from radar and seismic
     sounding data, Annals of Glaciology, 37, 317–324, https://doi.org/10.3189/172756403781815924, 2003.

515 Beraud, L., Cusicanqui, D., Rabatel, A., Brun, F., Vincent, C., and Six, D.: Glacier-wide seasonal and annual geodetic mass bal-
     ances from Pléiades stereo images: application to the Glacier d'Argentière, French Alps, Journal of Glaciology, 69, 525–537,
     https://doi.org/10.1017/jog.2022.79, 2022.

Bock, Y., Gourevitch, S. A., Counselman, III, C. C., King, R. W., and Abbot, R. I.: Interferometric analysis of GPS phase observations,
     Manuscripta Geodaetica, 11, 282–288, 1986.

520 Booth, A. D., Christoffersen, P., Schoonman, C., Clarke, A., Hubbard, B., Law, R., Doyle, S. H., Chudley, T. R., and Chalari, A.: Distributed
     Acoustic Sensing of Seismic Properties in a Borehole Drilled on a Fast-Flowing Greenlandic Outlet Glacier, Geophysical Research Letters,
     47, e2020GL088 148, https://doi.org/10.1029/2020GL088148, 2020.

Budd, W. F. and Jacka, T. H.: A review of ice rheology for ice sheet modelling, Cold Regions Science and Technology, 16, 107–144,
     https://doi.org/10.1016/0165-232X(89)90014-1, 1989.

525 Chandler, D., Hubbard, B., Hubbard, A., Murray, T., and Rippin, D.: Optimising ice flow law parameters using borehole deformation mea-
     surements and numerical modelling, Geophysical Research Letters, 35, https://doi.org/10.1029/2008GL033801, 2008.

Chauve, T., Montagnat, M., Dansereau, V., Saramito, P., Fourteau, K., and Tommasi, A.: A physically-based formulation for texture evolution
     during dynamic recrystallization. A case study for ice, Submitted, https://hal.science/hal-04231338, 2024a.

Chauve, T., Montagnat, M., Dansereau, V., Saramito, P., Fourteau, K., and Tommasi, A.: A physically-based formulation for texture evolution
530   during dynamic recrystallization. A case study of ice, Comptes Rendus. Mécanique, 352, 99–134, https://doi.org/10.5802/crmeca.243,
     2024b.

Cohen, D.: Rheology of ice at the bed of engabreen, Norway, Journal of Glaciology, 46, 611–621,
     https://doi.org/10.3189/172756500781832620, 2000.

Cuffey, K. M. and Paterson, W. S. B.: The physics of glaciers, Academic Press, Amsterdam, 4th ed. edn., 2010.

535 Doyle, S. H., Hubbard, B., Christoffersen, P., Young, T. J., Hofstede, C., Bougamont, M., Box, J. E., and Hubbard, A.: Physical Conditions
     of Fast Glacier Flow: 1. Measurements From Boreholes Drilled to the Bed of Store Glacier, West Greenland, Journal of Geophysical
     Research: Earth Surface, 123, 324–348, https://doi.org/10.1002/2017JF004529, 2018.

Duval, P.: The role of the water content on the creep rate of polycrystalline ice, IAHS Publ, 118, 29–33, 1977.

Endres, A. L., Murray, T., Booth, A. D., and West, L. J.: A new framework for estimating englacial water content and pore geometry using combined radar and seismic wave velocities, Geophysical Research Letters, 36, https://doi.org/10.1029/2008GL036876, 2009.

Fichtner, A., Hofstede, C., Gebraad, L., Zunino, A., Zigone, D., and Eisen, O.: Borehole fibre-optic seismology inside the Northeast Greenland Ice Stream, Geophysical Journal International, 235, 2430–2441, https://doi.org/10.1093/gji/ggad344, 2023.

Fürst, J. J., Durand, G., Gillet-Chaulet, F., Merino, N., Tavard, L., Mouginot, J., Gourmelen, N., and Gagliardini, O.: Assimilation of Antarctic velocity observations provides evidence for uncharted pinning points, The Cryosphere, 9, 1427–1443, https://doi.org/https://doi.org/10.5194/tc-9-1427-2015, 2015.

Gagliardini, O., Zwinger, T., Gillet-Chaulet, F., Durand, G., Favier, L., de Fleurian, B., Greve, R., Malinen, M., Martín, C., Råback, P., Ruokolainen, J., Sacchettini, M., Schäfer, M., Seddik, H., and Thies, J.: Capabilities and performance of Elmer/Ice, a new-generation ice sheet model, Geoscientific Model Development, 6, 1299–1318, https://doi.org/10.5194/gmd-6-1299-2013, 2013.

Gajek, W., Gräff, D., Hellmann, S., Rempel, A. W., and Walter, F.: Diurnal expansion and contraction of englacial fracture networks revealed by seismic shear wave splitting, Communications Earth & Environment, 2, 1–8, https://doi.org/10.1038/s43247-021-00279-4, 2021.

Gilbert, A., Gimbert, F., Thøgersen, K., Schuler, T. V., and Kääb, A.: A Consistent Framework for Coupling Basal Friction With Subglacial Hydrology on Hard-Bedded Glaciers, Geophysical Research Letters, 49, e2021GL097 507, https://doi.org/10.1029/2021GL097507, 2022.

Gilbert, A., Gimbert, F., Gagliardini, O., and Vincent, C.: Inferring the Basal Friction Law From Long Term Changes of Glacier Length, Thickness and Velocity on an Alpine Glacier, Geophysical Research Letters, 50, e2023GL104 503, https://doi.org/10.1029/2023GL104503, 2023.

Gimbert, F., Gilbert, A., Gagliardini, O., Vincent, C., and Moreau, L.: Do Existing Theories Explain Seasonal to Multi-Decadal Changes in Glacier Basal Sliding Speed?, Geophysical Research Letters, 48, 1–10, https://doi.org/10.1029/2021GL092858, 2021a.

Gimbert, F., Nanni, U., Roux, P., Helmstetter, A., Garambois, S., Lecointre, A., Walpersdorf, A., Jourdain, B., Langlais, M., Laarman, O., Lindner, F., Sergeant, A., Vincent, C., and Walter, F.: A multi-physics experiment with a temporary dense seismic array on the argentière Glacier, French Alps: The RESOLVE project, Seismological Research Letters, 92, 1185–1201, https://doi.org/10.1785/0220200280, 2021b.

Glen, J. W.: The creep of polycrystalline ice, Proceedings of the Royal Society of London. Series A. Mathematical and Physical Sciences, 228, 519–538, https://doi.org/10.1098/rspa.1955.0066, 1955.

Goldsby, D. L. and Kohlstedt, D. L.: Superplastic deformation of ice: Experimental observations, Journal of Geophysical Research: Solid Earth, 106, 11 017–11 030, https://doi.org/10.1029/2000JB900336, 2001.

Gudmundsson, G. H.: Basal-flow characteristics of a linear medium sliding frictionless over small bedrock undulations, Journal of Glaciology, 43, 71–79, https://doi.org/10.1017/s0022143000002823, 1997.

Gudmundsson, G. H., Bauder, A., Lüthi, M., Fischer, U. H., and Funk, M.: Estimating rates of basal motion and internal ice deformation from continuous tilt measurements, Annals of Glaciology, 28, 247–252, https://doi.org/10.3189/172756499781821751, 1999.

Hantz, D. and Llioutry, L.: Waterways, Ice Permeability at Depth, and Water Pressures at Glacier D'Argentière, French Alps, Journal of Glaciology, 29, 227–239, https://doi.org/10.3189/S0022143000008285, 1983.

Harper, J. T., Humphrey, N. F., Pfeffer, W. T., Huzurbazar, S. V., Bahr, D. B., and Welch, B. C.: Spatial variability in the flow of a valley glacier: Deformation of a large array of boreholes, Journal of Geophysical Research: Solid Earth, 106, 8547–8562, https://doi.org/10.1029/2000jb900440, 2001.

Hooke, R. L.: Structure and Flow in the Margin of the Barnes Ice Cap, Baffin Island, N.W.T., Canada, Journal of Glaciology, 12, 423–438, https://doi.org/10.3189/s0022143000031841, 1973.

Hooke, R. L., Pohjola, V. A., Jansson, P., and Kohler, J.: Intra-seasonal changes in deformation profiles revealed by borehole studies, Storglaciaren, Sweden, Journal of Glaciology, 38, 348–358, https://doi.org/10.1017/S0022143000002239, 1992.

Hooke, R. L. B. and Hanson, B.: Borehole deformation experiments, Barnes Ice Cap, Canada, Cold Regions Science and Technology, 12, 261–276, https://doi.org/10.1016/0165-232X(86)90039-X, 1986.

Hubbard, B. P., Hubbard, A., Mader, H. M., Tison, J. L., Grust, K., and Nienow, P. W.: Spatial variability in the water content and rheology of temperate glaciers: Glacier de Tsanfleuron, Switzerland, Annals of Glaciology, 37, 1–6, https://doi.org/10.3189/172756403781815474, 2003.

Jones, S. J. and Glen, J. W.: The effect of dissolved impurities on the mechanical properties of ice crystals, The Philosophical Magazine: A Journal of Theoretical Experimental and Applied Physics, 19, 13–24, https://doi.org/10.1080/14786436908217758, 1969.

Joubert, J.-L.: Stratigraphie de la glace tempérée à l'aide de la teneur en eau liquide., Comptes rendus académie des sciences, p. 3638, 1963.

Keller, A. and Blatter, H.: Measurement of strain-rate components in a glacier with embedded inclinometers, Journal of Glaciology, 58, 692–698, https://doi.org/10.3189/2012JoG11J234, 2012.

Law, R., Christoffersen, P., MacKie, E., Cook, S., Haseloff, M., and Gagliardini, O.: Complex motion of Greenland Ice Sheet outlet glaciers with basal temperate ice, Science Advances, 9, eabq5180, https://doi.org/10.1126/sciadv.abq5180, 2023.

Lee, I. R., Hawley, R. L., Bernsen, S., Campbell, S. W., Clemens-Sewall, D., Gerbi, C. C., and Hruby, K.: A novel tilt sensor for studying ice deformation: Application to streaming ice on Jarvis Glacier, Alaska, Journal of Glaciology, 66, 74–82, https://doi.org/10.1017/jog.2019.84, 2019.

Legchenko, A., Vincent, C., Baltassat, J. M., Girard, J. F., Thibert, E., Gagliardini, O., Descloitres, M., Gilbert, A., Garambois, S., Chevalier, A., and Guyard, H.: Monitoring water accumulation in a glacier using magnetic resonance imaging, The Cryosphere, 8, 155–166, https://doi.org/10.5194/tc-8-155-2014, 2014.

Lliboutry, L.: Une théorie du frottement du glacier sur son lit, Annales de Geophysique, 15, 250, 1959.

Lliboutry, L.: General theory of subglacial cavitation and sliding of temperate glaciers, Journal of Glaciology, 7, 21–58, 1968.

Lliboutry, L.: Permeability, Brine Content and Temperature of Temperate Ice, Journal of Glaciology, 10, 15–29, https://doi.org/10.3189/s002214300001296x, 1971.

Lliboutry, L.: Multivariate Statistical Analysis of Glacier Annual Balances, Journal of Glaciology, 13, 371–392, https://doi.org/10.3189/s0022143000023169, 1974.

Lliboutry, L. and Duval, P.: Various isotropic and anisotropic ices found in glaciers and polar ice caps and their corresponding rheologies, International Journal of Rock Mechanics and Mining Sciences & Geomechanics Abstracts, 22, 198, https://doi.org/10.1016/0148-9062(85)90267-0, 1985.

Lüthi, M., Funk, M., Iken, A., Gogineni, S., and Truffer, M.: Mechanisms of fast flow in Jakobshavn Isbræ, West Greenland: Part III. Measurements of ice deformation, temperature and cross-borehole conductivity in boreholes to the bedrock, Journal of Glaciology, 48, 369–385, https://doi.org/10.3189/172756502781831322, 2002.

Maier, N., Humphrey, N., Harper, J., and Meierbachtol, T.: Sliding dominates slow-flowing margin regions, Greenland Ice Sheet, Science Advances, 5, eaaw5406, https://doi.org/10.1126/sciadv.aaw5406, 2019.

Maier, N., Humphrey, N., Meierbachtol, T., and Harper, J.: Deformation motion tracks sliding changes through summer, western Greenland, Journal of Glaciology, pp. 1–10, https://doi.org/10.1017/jog.2021.87, 2021.

Maier, N., Gimbert, F., and Gillet-Chaulet, F.: Threshold response to melt drives large-scale bed weakening in Greenland, Nature, 607, 714–720, https://doi.org/10.1038/s41586-022-04927-3, 2022.

Marshall, H. P., Harper, J. T., Pfeffer, W. T., and Humphrey, N. F.: Depth-varying constitutive properties observed in an isothermal glacier, Geophysical Research Letters, 29, 61–1–61–4, https://doi.org/10.1029/2002GL015412, 2002.

Montagnat, M. and Duval, P.: The viscoplastic behaviour of ice in polar ice sheets: experimental results and modelling, Comptes Rendus Physique, 5, 699–708, https://doi.org/10.1016/j.crhy.2004.06.002, 2004.

Mosbeux, C., Gillet-Chaulet, F., and Gagliardini, O.: Comparison of adjoint and nudging methods to initialise ice sheet model basal conditions, Geosci. Model Dev., 9, 2549–2562, https://doi.org/10.5194/gmd-9-2549-2016, 2016.

Murray, T., Stuart, G. W., Fry, M., Gamble, N. H., and Crabtree, M. D.: Englacial water distribution in a temperate glacier from surface and borehole radar velocity analysis, Journal of Glaciology, 46, 389–398, https://doi.org/10.3189/172756500781833188, 2000.

Murray, T., Booth, A., and Rippin, D. M.: Water-content of Glacier-ice: Limitations on estimates from velocity analysis of surface ground-penetrating radar surveys, Journal of Environmental and Engineering Geophysics, 12, 87–99, https://doi.org/10.2113/JEEG12.1.87, 2007.

Nanni, U., Gimbert, F., Roux, P., and Lecointre, A.: Observing the subglacial hydrology network and its dynamics with a dense seismic array, Proceedings of the National Academy of Sciences of the United States of America, 118, 1–7, https://doi.org/10.1073/pnas.2023757118, 2021.

Nye, J. F.: The Flow of a Glacier in a Channel of Rectangular, Elliptic or Parabolic Cross-Section, Journal of Glaciology, 5, 661–690, https://doi.org/10.3189/s0022143000018670, 1965.

Ogier, C., Manen, D.-J. v., Maurer, H., Räss, L., Hertrich, M., Bauder, A., and Farinotti, D.: Ground penetrating radar in temperate ice: englacial water inclusions as limiting factor for data interpretation, Journal of Glaciology, pp. 1–12, https://doi.org/10.1017/jog.2023.68, 2023.

Perutz, M. F.: Direct Measurement of the Velocity Distribution in a Vertical Profile Through a Glacier, Journal of Glaciology, 1, 382–383, https://doi.org/10.3189/s0022143000012594, 1949.

Pettersson, R., Jansson, P., and Blatter, H.: Spatial variability in water content at the cold-temperate transition surface of the polythermal Storglaciären, Sweden, Journal of Geophysical Research: Earth Surface, 109, n/a–n/a, https://doi.org/10.1029/2003jf000110, 2004.

Rabatel, A., Sanchez, O., Vincent, C., and Six, D.: Estimation of Glacier Thickness From Surface Mass Balance and Ice Flow Velocities: A Case Study on Argentière Glacier, France, Frontiers in Earth Science, 6, https://doi.org/10.3389/feart.2018.00112, 2018.

Rathmann, N. M. and Lilien, D. A.: Inferred basal friction and mass flux affected by crystal-orientation fabrics, Journal of Glaciology, 68, 236–252, https://doi.org/10.1017/jog.2021.88, 2022.

Raymond, C.: Flow in a Transverse Section of Athabasca Glacier, Alberta, Canada, Journal of Glaciology, 10, 55–84, https://doi.org/10.3189/s0022143000012995, 1971.

Ryser, C., Lüthi, M. P., Andrews, L. C., Hoffman, M. J., Catania, G. A., Hawley, R. L., Neumann, T. A., and Kristensen, S. S.: Sustained high basal motion of the Greenland ice sheet revealed by borehole deformation, Journal of Glaciology, 60, 647–660, https://doi.org/10.3189/2014JoG13J196, 2014.

Röthlisberger, H.: Water Pressure in Intra- and Subglacial Channels *, Journal of Glaciology, 11, 177–203, https://doi.org/10.3189/S0022143000022188, 1972.

Schoof, C.: Ice-sheet acceleration driven by melt supply variability, Nature, 468, 803–806, https://doi.org/10.1038/nature09618, 2010.

Sergeant, A., Chmiel, M., Lindner, F., Walter, F., Roux, P., Chaput, J., Gimbert, F., and Mordret, A.: On the Green's function emergence from interferometry of seismic wave fields generated in high-melt glaciers: Implications for passive imaging and monitoring, The Cryosphere, 14, 1139–1171, https://doi.org/10.5194/tc-14-1139-2020, 2020.

Shreve, R. and Sharp, R.: Internal Deformation and Thermal Anomalies in Lower Blue Glacier, Mount Olympus, Washington, U.S.A., Journal of Glaciology, 9, 65–86, https://doi.org/10.3189/S0022143000026800, 1970.

Togaibekov, A., Gimbert, F., Gilbert, A., and Walpersdorf, A.: Observing and Modeling Short-Term Changes in Basal Friction During Rain-Induced Speed-Ups on an Alpine Glacier, Geophysical Research Letters, 51, e2023GL107 999, https://doi.org/10.1029/2023GL107999, 2024.

Vallon, M., Petit, J.-R., and Fabre, B.: Study of an Ice Core to the Bedrock in the Accumulation zone of an Alpine Glacier, Journal of Glaciology, 17, 13–28, https://doi.org/10.3189/S0022143000030677, 1976.

Vincent, C. and Moreau, L.: Sliding velocity fluctuations and subglacial hydrology over the last two decades on Argentière glacier, Mont Blanc area, Journal of Glaciology, 62, 805–815, https://doi.org/10.1017/jog.2016.35, 2016.

Vincent, C., Fischer, A., Mayer, C., Bauder, A., Galos, S. P., Funk, M., Thibert, E., Six, D., Braun, L., and Huss, M.: Common climatic signal from glaciers in the European Alps over the last 50 years, Geophysical Research Letters, 44, 1376–1383, https://doi.org/10.1002/2016GL072094, 2017.

Vincent, C., Gilbert, A., Walpersdorf, A., Gimbert, F., Gagliardini, O., Jourdain, B., Roldan Blasco, J. P., Laarman, O., Piard, L., Six, D., Moreau, L., Cusicanqui, D., and Thibert, E.: Evidence of Seasonal Uplift in the Argentière Glacier (Mont Blanc Area, France), Journal of Geophysical Research: Earth Surface, 127, e2021JF006 454, https://doi.org/10.1029/2021JF006454, 2022.

Vivian, R. and Bocquet, G.: Subglacial Cavitation Phenomena Under the Glacier D'Argentière, Mont Blanc, France, Journal of Glaciology, 12, 439–451, https://doi.org/10.3189/S0022143000031853, 1973.

Weertman, J.: On the Sliding of Glaciers, Journal of Glaciology, https://doi.org/10.3189/s0022143000024709, 1957.

Weertman, J.: CREEP DEFORMATION OF ICE, Annual Review of Earth and Planetary Sciences, 11, 215–240, https://doi.org/10.1146/annurev.ea.11.050183.001243, 1983.

Willis, I., Mair, D., Hubbard, B., Nienow, P., Fischer, U. H., and Hubbard, A.: Seasonal variations in ice deformation and basal motion across the tongue of Haut Glacier d'Arolla, Switzerland, Annals of Glaciology, 36, 157–167, https://doi.org/10.3189/172756403781816455, 2003.

Young, T. J., MartÃn, C., Christoffersen, P., Schroeder, D. M., Tulaczyk, S. M., and Dawson, E. J.: Rapid and accurate polarimetric radar measurements of ice crystal fabric orientation at the Western Antarctic Ice Sheet (WAIS) Divide ice core site, The Cryosphere, 15, 4117–4133, https://doi.org/10.5194/tc-15-4117-2021, 2021.

Zryd, A.: Conditions dans la couche basale des glaciers tempérés: contraintes, teneur en eau et frottement intérieur, Ph.D. thesis, ETH, 1991.